nature communications

Article

https://doi.org/10.1038/s41467-025-64962-2

Fast-switching dual-cathode electrochromic smart windows for year-round building energy savings

Received: 8 March 2025

Accepted: 29 September 2025

Published online: 30 October 2025

Check for updates

Fayong Sun[1], Raksha Pal[1], Soo Yeon Eom[1], Jae Won Choi[1], Wei Zhang[1], Beomjin Jeong[1,2] & Jong S. Park[1,2,3]

For dual-band electrochromic smart windows to achieve widespread adoption, challenges such as slow switching, poor stability, and high power consumption must be addressed. This study introduces a polyviologen|zinc mesh|$WO_3 \cdot 2H_2O$ electrochromic energy storage device (EESD) with a PEDOT: PSS layer to enhance conductivity and prevent polyviologen degradation. By utilizing a dual-cathode design, the EESD enables fast switching and operates in four distinct modes—transparent, visible colored, near-infrared colored, and fully colored—allowing adaptive light regulation (320–2500 nm) to optimize energy efficiency across different seasons and times of day. Its self-operating and energy recovery features achieve zero energy consumption while maintaining functionality similar to conventional glass. Simulations indicate that a large-scale deployment across the U.S. can save 66.87 billion MWh, amounting to $7.35 trillion, and reduce CO_2 emissions by 66.94 billion tons. With its rapid switching, long-term durability, and scalability, this device presents significant economic and environmental advantages for real-world applications.

Numerous reports indicate that over 30% of energy consumption and 10% of greenhouse gas emissions stem from building energy use, with a large portion dedicated to heating, ventilation, and air conditioning (HVAC) systems[1]. The widespread use of building glass, particularly in curtain walls, is a major driver of increased HVAC energy consumption. Traditional windows allow heat and light to pass freely, making them one of the least energy-efficient components in buildings[2]. In this context, electrochromic (EC) smart windows have emerged as a promising technological solution to address this issue[3–5]. Ideal smart windows should be able to dynamically adjust the transmittance of light in both the visible (380–780 nm) and near-infrared (NIR, 780–2520 nm) ranges under different voltage levels, enabling intelligent management of indoor light and heat in response to varying external conditions[6,7].

Zinc-based aqueous electrochromic energy storage devices (EESDs) have garnered widespread attention in recent years due to their low cost, safety, high performance, and energy-saving characteristics[8–11]. Some researchers have successfully developed EESDs that integrate dual EC electrodes with a zinc anode, enabling independent light transmittance control in visible and NIR regions[5,12–14]. Additionally, these devices often featured energy storage capabilities that could further improve energy efficiency. However, their design commonly incorporated a center-placed zinc foil, which, being opaque, could not be extensively integrated. This restricted its contact with the electrolyte, making the devices suitable only for non-solid-state and small-area applications[14–17]. A new approach is needed to enable the solid-state architecture and large-scale fabrication of such devices, bridging the gap from laboratory-scale research to commercial application.

Viologen is a class of reversible redox-active materials commonly used as cathode materials in electrochromic devices (ECDs)[18,19]. In energy storage applications, viologen was known for its high

[1]School of Chemical Engineering, Pusan National University, Busan, Korea. [2]Department of Organic Material Science and Engineering, Pusan National University, Busan, Korea. [3]Research Institute for Convergence of Biomedical Science and Technology, Pusan National University Yangsan Hospital, Yangsan, Korea. e-mail: jongpark@pusan.ac.kr

reversibility, long lifespan, high solubility, adjustable redox potential, environmental safety, and low cost[19,20]. In the EC field, it has been frequently researched due to its significant color change, high coloration efficiency (CE), robust reversibility and stability, and ease of molecular modification and functionalization[21–24]. However, amidst the development of various materials for EESDs, studies related to viologen-based EESDs are limited[25].

Previously, our laboratory reported on viologen-zinc ion EESDs, which showed promising results, but challenges such as slow switching speed, low CE, and inability to scale up remained unresolved[16,26]. The fundamental issue lies in the fact that viologen is a fundamentally non-conductive organic material, so in ECDs, it is typically included in ion gels to make direct contact with the anode material to improve response speed[27,28]. However, this design structure is not conducive to energy storage. To enhance the energy storage performance of viologen-based EESDs, some studies have suggested mixing viologen with other materials, such as carbon black and polymers, creating separate films, and isolating the anode with an electrolyte[29–31]. The main limitation of this design is the compromised electrochromic performance, as the resulting devices lose transparency, exhibit uneven coloration, and experience significantly slower response times. Polymeric structures were suggested, but several challenges remain unresolved, including limited transparency, low conductivity, and instability caused by swelling and corrosion[32,33]. In the field of viologen-based EESDs, therefore, there is a need for a new approach that balances both aspects of performance to drive research progress.

Here, we propose fast-switching transparent viologen-based EESDs with dual cathodes exhibiting four distinct EC modes and achieving visible-NIR dual-band EC energy storage functionality. Transparent polyviologen (PV) and $WO_3 \cdot 2H_2O$ are articulately chosen as cathodic materials on both terminals, ingeniously adopting PEDOT:PSS as a protective and proton-providing layer for polyviologen[34]. Impressively, PEDOT:PSS not only effectively prevents the polyviologen from being degraded but also acts as a proton source to increase the speed of the reversible redox reaction and enhance the interfacial contact conductivity. Combined with the uniform electric field produced by the UV-cured solid-state electrolyte-coated zinc mesh[35], which is highly transparent, the resulting EESDs exhibit high transparency, fast switching, exceptional capacitive contribution, uniform coloration, and strong potential for large-scale manufacturing. The current approach leads to significant energy-saving effects in two ways. First, the device has a high energy storage capacity, allowing it to return the energy used to drive it. Furthermore, the device features self-coloring and self-bleaching capability, achieving zero energy consumption. Second, the dual-band, four-mode EESDs, when used as a smart window for buildings, can regulate the transmission of visible and NIR light, enabling intelligent light-heat management and significantly reducing HVAC energy consumption. Experimental and simulation tests for all-day, year-round, and across the United States demonstrate that smart building windows can effectively regulate the light and heat entering indoor spaces, accounting for 10% energy savings compared to conventional low-emissivity (low-E) glass.

Results

Design and working principles of the devices

We propose conceptual EESD smart windows with four distinct modes: transparent, visible colored, NIR colored, and fully colored, designed to adapt to different times of the day, seasons, and regional weather conditions. The structure of the polyviologen|Zn mesh|$WO_3 \cdot 2H_2O$ device is illustrated in Fig. 1. It features a nearly symmetrical configuration, with polyviologen/PEDOT:PSS and $WO_3 \cdot 2H_2O$ cathodes attached to ITO-PET substrates on the top and bottom, respectively, enabling independent control over visible and NIR light transmission. The central layer consists of a UV-cured solid-state aqueous electrolyte-coated zinc mesh, which serves as the anode. This architecture allows for controllable self-charging (bleaching) and discharging (coloration) independently in visible and NIR regions. When sunlight enters a building, the visible light provides illumination while generating significant heat, whereas NIR light contributes solely to heat gain without enhancing visibility. Thus, our smart window was designed to intelligently regulate these two spectral bands, optimizing indoor brightness and temperature control. In cold weather (Fig. 1a), the $WO_3 \cdot 2H_2O$ layer remains neutral and transparent, allowing NIR light to enter and heat the interior. Meanwhile, the polyviologen layer can either remain transparent to maximize indoor brightness and warmth or switch to colored mode for privacy protection, functioning as a dynamic "blind". During hot conditions (Fig. 1b), the $WO_3 \cdot 2H_2O$ layer darkens, blocking NIR light to reduce heat gain. Similarly, the polyviologen layer can be adjusted based on indoor brightness and temperature needs. For example, at midday, when sunlight is intense, polyviologen switches to colored mode to reduce both visible light and heat, maintaining a comfortable indoor environment. On cloudy days, at dawn, or during dusk, it remains transparent to maximize natural lighting. By dynamically modulating sunlight transmission, this smart window effectively reduces the reliance on artificial lighting and HVAC systems, significantly lowering building energy consumption.

Electrochemical properties of the polyviologen | Zn mesh | ECDs

In realizing the dual-cathode, four-mode smart window, we envisaged the EESD based on a polyviologen|Zn mesh structure. To achieve this, we specifically designed and synthesized a highly transparent polyviologen, with characterization as detailed in Methods. The sprayed polyviologen thin film on ITO-PET exhibited over 90% optical transmittance, surpassing conventional EC material films (Fig. S1, Supplementary Information)[36,37]. To address the inherent drawbacks of low response speed due to low conductivity and poor stability due to swelling in polyviologen, the conductive polymer, PEDOT:PSS, was introduced as a protective and enhancement layer. The device architecture is illustrated in Fig. 2a, while Fig. 2b displays the morphology and thickness of the corresponding layers, with the polyviologen layer measuring 3.9 μm and the PEDOT:PSS layer measuring 80 nm. The Zn mesh with a wire diameter of 36 μm maintained high transmittance, with an average optical transmittance of 88.5%, as shown in Fig. S2 (Supplementary Information). The electrolyte-coated Zn mesh also retained high transparency, with minor absorption dips at 1437 nm, 1930 nm, and 2500 nm, indicating water absorption (Fig. S3, Supplementary Information). PEDOT:PSS was chosen due to its high electrical conductivity, stability, and low redox potential, mainly benefiting from its relatively low interfacial resistance with aqueous zinc-ion electrolytes[38–40]. During the charging and discharging process, reversible Zn deposition and dissolution occur at the Zn mesh anode, while the $PEDOT^+$ and polyviologen cathodes undergo redox reactions, as described by the following electrochemical equations:

$$\text{Anode reaction:} \quad Zn \leftrightarrow Zn^{2+} + 2e^- \tag{1}$$

$$\text{Cathode reactions:} \quad PEDOT^+(\text{transparent}) + e^- \leftrightarrow PEDOT(\text{light blue}) \tag{2}$$

$$PV^{2+}(\text{transparent}) + e^- \leftrightarrow PV^{+\cdot}(\text{deep blue} - \text{violet}) \tag{3}$$

The chemical structure changes of polyviologen during this redox process are depicted in Fig. 2c.

Cyclic voltammetry (CV) tests were performed to analyze their electrochemical performance (Fig. 2d). At a scan rate of 2 mV s^{-1}, the device without the PEDOT:PSS layer exhibits only one pair of a reduction peak at −0.66 V and an oxidation peak at −0.41 V, corresponding to the reversible process transitioning from PV^{2+} to $PV^{+\cdot}$ and

https://doi.org/10.1038/s41467-025-64962-2

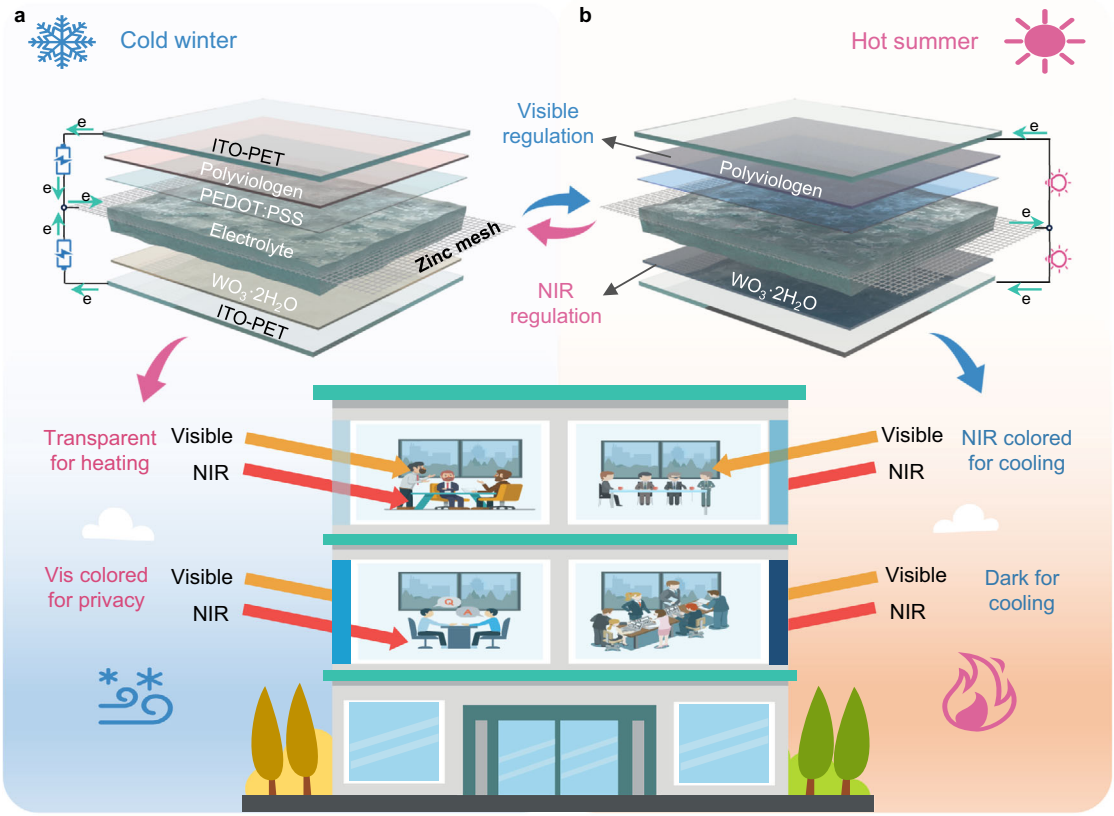

Fig. 1 | Schematic diagram of the design and working principle of the devices. a The polyviologen|Zn mesh|$WO_3 \cdot 2H_2O$ EESD and its working principle for regulating visible and NIR light in winter. **b** The polyviologen|Zn mesh|$WO_3 \cdot 2H_2O$ EESD in the coloring state and its working principle for regulating visible and NIR light in summer.

back to PV^{2+}. For the polyviologen|Zn mesh EESD with the PEDOT:PSS layer, besides the oxidation (−0.40 V) and reduction peaks (−0.58 V) of polyviologen, there is an additional minor oxidation (−0.88 V) and reduction (−1.05 V) pair associated with PEDOT:PSS (Fig. 2e). Thus, during reduction, the voltage decreases from the neutral charging state at −1.2 V to −1.05 V, causing $PEDOT^+$ to convert into PEDOT. Attributed to the enhanced ionic conduction and the presence of a potential step provided by the PEDOT:PSS layer, faster reduction of polyviologen occurs at −0.58 V, which is reflected in a significant increase in peak current.

At various scan rates from 1 to 10 mV s^{-1}, both the anode (I_{pa}) and cathode (I_{pc}) peak currents increased with the square root of the scan rate but did not show a linear correlation, indicating that the device's behavior is not solely diffusion-controlled (Fig. 2f). The devices with the PEDOT:PSS layer exhibited higher peak currents, with a significant increase in peak current as the square root of the scan rate increased, suggesting an enhancement in the electron transfer rate. Further analysis of the charge storage mechanism was conducted. Based on the equation $i = av^b$ [41], a plot of log(i) versus log(v) was generated, where i and v represent the peak current and scan rate, respectively (Fig. 2g). The calculated b values are approximately 0.85, falling between 0.5 (diffusion-controlled) and 1.0 (surface capacitive control). This value indicates that the PEDOT:PSS layer does not affect the dual control mechanism of charge storage, which is governed by both diffusion and surface capacitance. To further elucidate the contributions of diffusion and capacitive control, the capacitive contribution at various scan rates was calculated. As shown in Fig. 2h, the results reveal that capacitive contributions dominate, increasing from 65.5% to 85.7% as the scan rate increases, with the PEDOT:PSS layer having no significant impact on this behavior. It should be noted that, with such a high capacitive contribution, the current EESDs demonstrate exceptional surface-controlled charge storage and exceptional high-rate performance.

The electrochemical impedance of the device was measured (Fig. 2i), and an equivalent circuit was employed for quantitative analysis of the impedance. In the equivalent circuit, the intersection on the real axis represents the internal resistance (R_s), while the diameter of the semicircle corresponds to the interfacial charge transfer resistance (R_{ct}). The results indicate that the presence or absence of the PEDOT:PSS layer does not affect the internal resistance of the electrolyte, which remains around 30 Ω. However, the PEDOT:PSS layer significantly influences the interfacial resistance, reducing it from 1356.7 Ω to 532.3 Ω. This result further confirms the role of the PEDOT:PSS layer in enhancing the electron transfer rate.

Electrochromic properties of the polyviologen | Zn mesh | ECDs

The PEDOT:PSS layer enhances the electrochemical performance, leading to a noticeable improvement in the electrochromic properties. When the transmittance was measured at various voltages ranging from −1.5 V to −0.1 V, the PEDOT:PSS layer did not impact the transmittance in its transparent state, which remains around 67.63% (Fig. 3a, b). However, a considerable difference is observed in the colored state, with the device containing the PEDOT:PSS layer showing a transmittance contrast of 64.23%, compared to just 44.41% for the device without it. Photographs of polyviologen|Zn mesh EESDs with PEDOT:PSS during the discharge (coloring) and charging (bleaching) processes are presented (Fig. 3c). The response speed of the two devices also exhibits a notable difference (Fig. 3d). The coloring and bleaching times of the device without the PEDOT:PSS layer are 30.1 s and 38.2 s, respectively. In comparison, aided by the enhanced ion migration and electron transfer of the PEDOT:PSS layer, the device achieved an astonishingly fast switching times of

https://doi.org/10.1038/s41467-025-64962-2

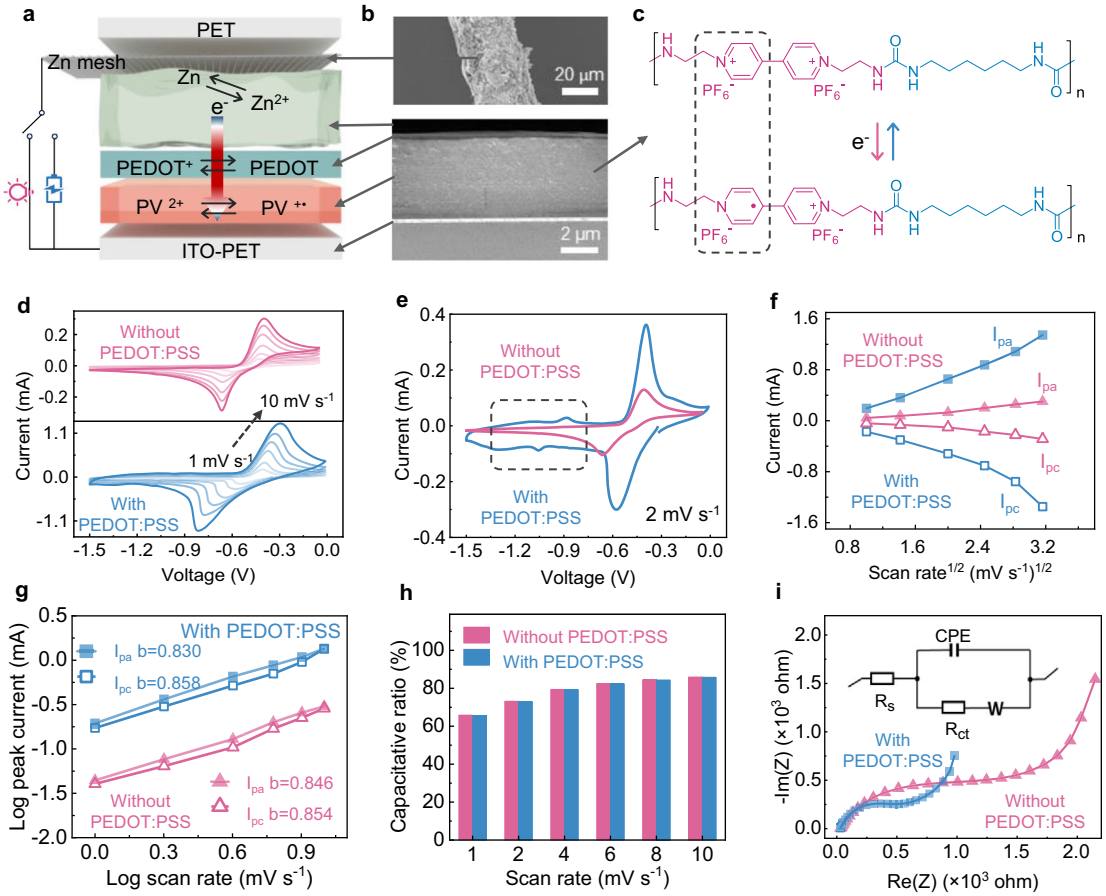

Fig. 2 | Comparative analysis of electrochemical properties. a Schematic diagram of the structure and working principle of the polyviologen|Zn mesh EESD. **b** Corresponding SEM images of the electrolyte-coated zinc mesh and the cross-section of EESD. **c** The chemical structure of polyviologen and its redox mechanism. **d** Cyclic voltammetry curves of the polyviologen|Zn mesh EESDs with and without PEDOT:PSS at different scan rates. **e** Cyclic voltammetry curves of the polyviologen|Zn mesh EESDs with and without PEDOT:PSS at a scan rate of 2 mV s^{-1}. **f** Linear plots of I_{pa} and I_{pc} versus the square root of applied voltage from cyclic voltammetry tests. **g** Calculation of b value from anodic and cathodic peaks of cyclic voltammetry tests. **h** Percentage of the capacitive contribution of the polyviologen|Zn mesh EESDs with and without PEDOT:PSS at different scan rates. **i** Nyquist plots of the two kinds of EESDs (the inset shows the corresponding fitted circuit).

1.6 s for coloration and 0.8 s for bleaching. To the best of our knowledge, this is one of the few reports in which a viologen-based EC device has achieved a response time of less than one second[28,42,43]. The darker color in the colored state results in a higher optical density, thereby increasing the coloration efficiency from 137.10 to 389.44 C cm^{-2} (Fig. 3e). The PEDOT:PSS layer also offers protective benefits for the polyviologen layer by preventing direct contact with water and zinc ions in the electrolyte, effectively reducing water-induced swelling and ion erosion of polyviologen. This protective effect is evident in the long-term cycling stability test (Fig. 3f). After 6600 s of cyclic operations, the device with the PEDOT:PSS layer maintains 90.58% of its ΔT, while the device without it retains only 57.03%.

Moreover, the PEDOT: PSS layer dramatically enhances the energy storage capacity of viologen-based EESDs by promoting the involvement of more polyviologen molecules in redox reactions. In the discharge test (Fig. 3g), the devices with and without the PEDOT: PSS layer show capacities of 141.9 and 73.2 mAh m^{-2}, respectively, at 0.5 mA cm^{-2}. The capacity measurements at varying current densities revealed similarly significant improvements (Fig. 3h). A comprehensive performance comparison between our device and other zinc-based EESDs, presented in a radar chart (Fig. 3i), highlights the competitive overall performances of the polyviologen|Zn mesh EESD with PEDOT:PSS, particularly excelling in response speed and coloration efficiency (Table S1, Supplementary Information)[8,13–16,44,45].

Electrochromic properties of the polyviologen | Zn mesh | $WO_3 \cdot 2H_2O$ EESD

In contrast to the zinc foil, the zinc mesh offers the benefit of preserving transparency and ensuring a uniform electric field while functioning on both terminal sides. This advantage allows for the innovative design of a large-area device featuring a double EC cathode structure on both sides and a central zinc mesh anode. Utilizing this configuration, combined with the NIR transmittance modulation of $WO_3 \cdot 2H_2O$[46], we implemented a four-mode functioning EESD that can freely control visible and NIR light (Fig. 4a). By separately managing the coloration of $WO_3 \cdot 2H_2O$ for NIR light and polyviologen for visible light, four smart window operation modes were realized: transparent, visible colored, NIR colored, and fully colored. The transmittance spectra from 320 to 2500 nm for the four modes are shown in Fig. 4b. The device in transparent mode demonstrates high transmittance in the visible and NIR bands from 380 to 2500 nm. In the visible colored mode, the device displays intense coloration in the 380 to 1000 nm range while maintaining high transmittance from 1000 to 2500 nm. In contrast, the NIR colored mode shows the opposite transmittance patterns, and the fully colored mode exhibits low transmittance throughout the 320 to 2500 nm range. At representative wavelengths of 600 nm (visible) and 1800 nm (NIR), the device demonstrated transmittance contrasts of 57.53% and 43.76%. All four models exhibit low transmittance in the

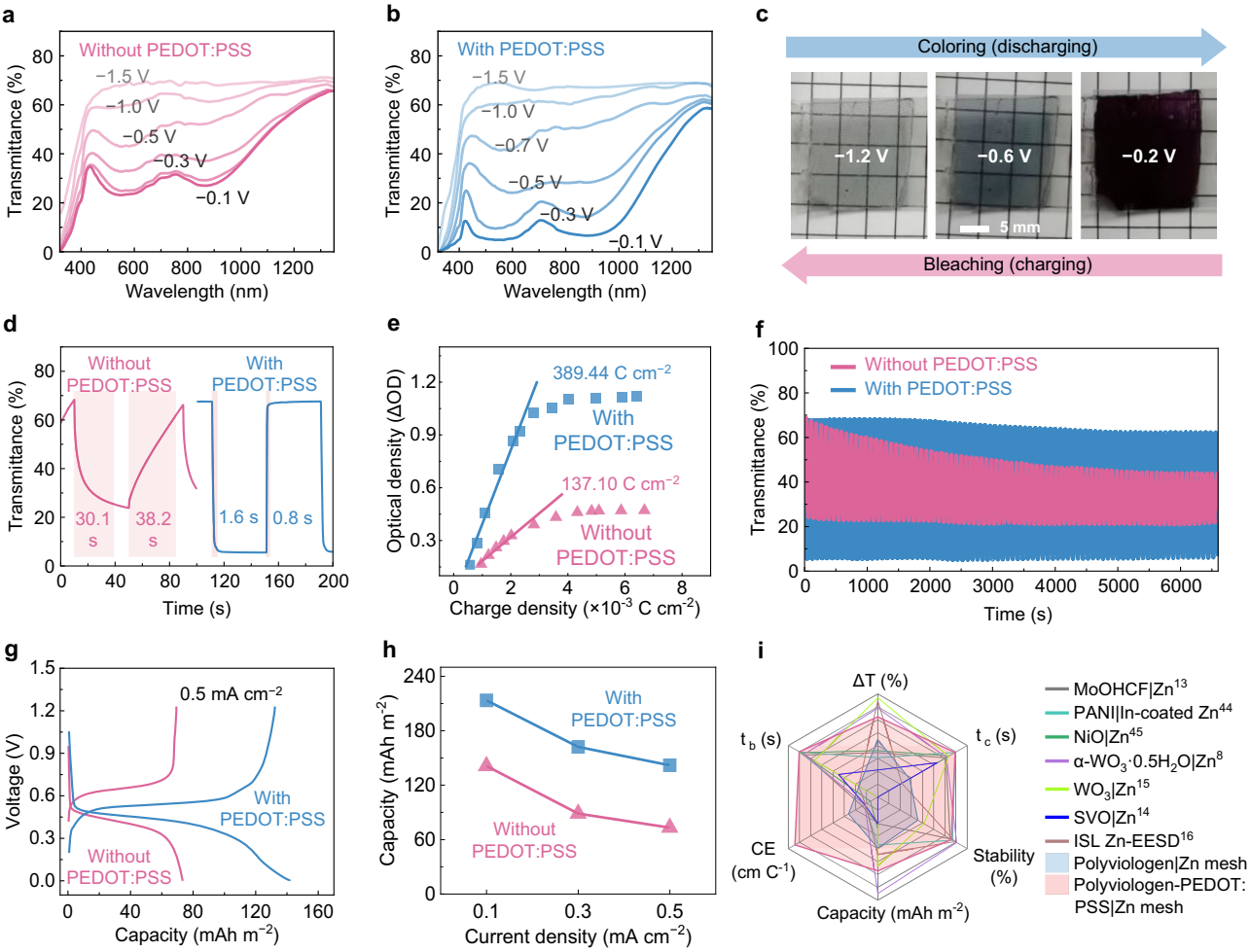

Fig. 3 | Comparison of electrochromic and energy storage properties. **a** Transmittances of the polyviologen|Zn mesh device without PEDOT:PSS at different voltages. **b** Transmittances of the device with PEDOT:PSS at various voltages. **c** Photographs of the state of the polyviologen|Zn mesh EESD with PEDOT:PSS at −1.2, −0.6, and −0.2 V. **d** Switching times of the polyviologen|Zn mesh EESDs without and with PEDOT:PSS (− 0.1 and −2.0 V, 40 s intervals). **e** Variation of the optical density (ΔOD) versus the charge density. **f** Kinetic stability of two kinds of EESDs (−0.1 and −2.0 V, 40 s intervals). **g** The discharge capacity of the polyviologen|Zn mesh EESDs without and with PEDOT:PSS at 0.5 mA cm^{-2}. **h** The corresponding discharge capacity at 0.1, 0.3, and 0.5 mA cm^{-2}. **i** Radar plot of the performance comparison of the polyviologen|Zn mesh EESD with other zinc EC energy storage devices.

ultraviolet (UV) region from 320 to 380 nm, blocking UV rays from reaching the human body. Actual photos of the four modes are shown in Fig. 4c (2.5 × 2.5 cm^2), and large-area device fabrication has also been demonstrated (10 × 10 cm^2, Figure S4, Supplementary Information).

The integrated optical transmittance (T) and solar irradiance-weighted transmittance (T′) of the polyviologen|Zn mesh|$WO_3 \cdot 2H_2O$ EESD were calculated for the visible (380–780 nm), NIR (780–2500 nm), and entire solar spectrum (380–2500 nm) regions. The results are presented in Fig. 4d and Table S2 (Supplementary Information). It is evident that the visible colored and NIR colored modes precisely regulate the transmission or blocking of solar light and radiation within respective spectral ranges. Meanwhile, the transparent and fully colored modes regulate solar radiation transmittance across the spectrum, with 54.75% and 2.34%, respectively, effectively controlling full-spectrum light transmittance.

The polyviologen and $WO_3 \cdot 2H_2O$ layers are connected to the Zn mesh via two separate electrochemical circuits. When the device is switched to the colored state by selectively linking the Zn mesh to each cathode, redox reactions occur independently within each circuit. Specifically, a reversible redox reaction takes place in the polyviologen|Zn circuit, while the $WO_3 \cdot 2H_2O$ | Zn circuit simultaneously undergoes the following reaction sequence:

$$\text{Anode reaction:} \quad Zn \leftrightarrow Zn^{2+} + 2e^- \tag{4}$$

$$\text{Cathode reaction:} \quad WO_3 \cdot 2H_2O\,(\text{transparent}) + xZn^{2+} + 2xe^- \leftrightarrow ZnxWO_3 \cdot 2H_2O\,(\text{blue}) \tag{5}$$

Each cathode operates through its redox mechanism without interference. This is further supported by the nearly unchanged EC performance observed in subsequent tests.

The response times of the polyviologen|Zn mesh|$WO_3 \cdot 2H_2O$ EESD from transparent to fully colored mode were evaluated at 600 nm and 1800 nm, representing the visible and NIR regions, respectively (Fig. 4e). Since polyviologen and $WO_3 \cdot 2H_2O$ undergo transmittance changes in respective spectral ranges, the switching at 600 nm and 1800 nm reflects the behavior of polyviologen and $WO_3 \cdot 2H_2O$ -based Zn mesh EESDs, respectively. The results show an ultrafast bleaching time of 0.8 s and a slightly delayed coloration time of 1.8 s at 600 nm, while at 1800 nm, the switching times are 3.2 s and 1.6 s, substantially outperforming most tungsten oxide-based devices[47]. Additionally, the coloration efficiency at 600 nm and 1800

https://doi.org/10.1038/s41467-025-64962-2

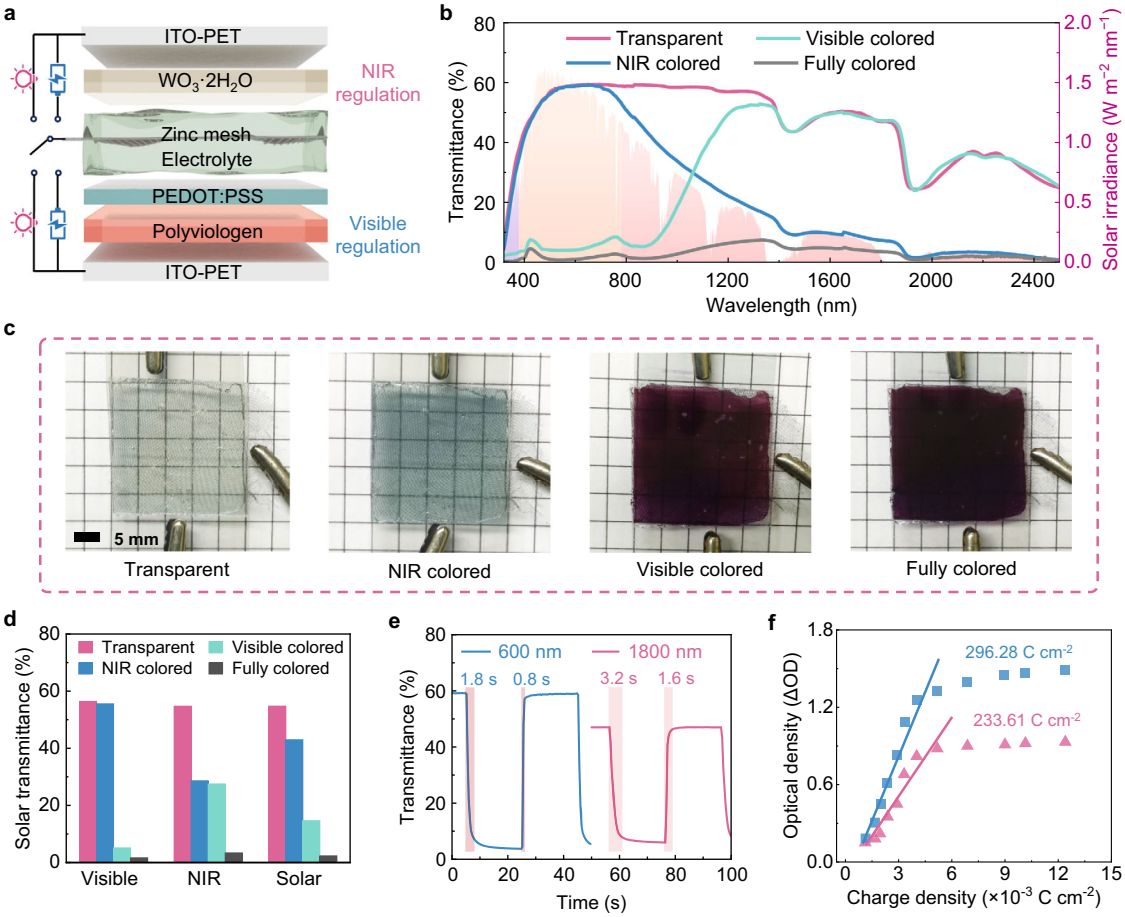

Fig. 4 | Electrochromic properties of the polyviologen|Zn mesh|$WO_3 \cdot 2H_2O$ EESD. **a** Schematic diagram of the structure and working principle of the polyviologen|Zn mesh|$WO_3 \cdot 2H_2O$ EESD. **b** Transmittance curves of the polyviologen|Zn mesh|$WO_3 \cdot 2H_2O$ EESD in the wavelength range from 320 to 2500 nm in transparent, visible colored, NIR colored, and fully colored states, with the standard solar spectrum (AM 1.5 G) in the background. **c** Photographs of the device in the corresponding states, device size: 2.5 × 2.5 cm^2. **d** Integrated solar irradiance transmittance (T′) of this device in the visible light (380–780 nm), NIR (780–2500 nm), and total solar irradiation (380–2500 nm) in the four different states. **e** The coloring and bleaching response times at 600 nm and 1800 nm (−0.1 and −2.0 V, 20 s intervals). **f** Variation of the optical density (ΔOD) versus the charge density at 600 nm and 1800 nm.

nm was obtained, yielding values of 296.28 and 233.61 C cm^{-2}, respectively (Fig. 4f). The driving dual cathode coloration increases the charge density, which causes a tweak in CE values; however, these values remain highly competitive compared to most previous studies[48,49]. The two independent circuits exhibit long-term cycling stability, operating continuously for 6,000 s with negligible performance degradation (Fig. S5, Supplementary Information). Both the polyviologen|Zn and $WO_3 \cdot 2H_2O$ | Zn circuits demonstrated a bistability capability, maintaining their colored states for approximately 30 min after disconnection (Fig. S6, Supplementary Information). This behavior is beneficial for enhancing the energy-saving potential of the smart window.

Energy consumption, energy recovery, and self-operating capability

Energy consumption and energy return are key performance indicators for evaluating EESDs, playing a crucial role in energy conservation and emission reduction[50,51]. The energy required to fully charge the polyviologen and $WO_3 \cdot 2H_2O$ cathodes with the Zn mesh anode and the energy that can be fully discharged were estimated. The percentage ratio between these values represents the energy return efficiency. As shown in Fig. 5a, a fully discharged polyviologen|Zn mesh circuit was initially subjected to a potentiostatic charging process at −2.0 V for 60 s (bleaching process), during which a total energy input of 132.50 mWh m^{-2} was recorded (Fig. S7a, Supplementary Information). The device was then galvanostatic discharged under 0.3 mA cm^{-2} (coloring process), releasing a total energy output of 58.89 mWh m^{-2} (Fig. S7b, Supplementary Information). Finally, an additional potentiostatic discharge at 0 V for 60 s was carried out to complete the final coloring process, consuming a negligible amount of energy, approximately 0.0018 mWh m^{-2} (Fig. S7c, Supplementary Information). Overall, the charge-discharge cycle consumed 132.5018 mWh m^{-2} and delivered an energy output of 58.89 mWh m^{-2}, yielding an energy return efficiency of 44.4%. Similarly, the energy return efficiency of the $WO_3 \cdot 2H_2O$ | Zn mesh circuit was determined to be 31.0% (Fig. 5b and S7d–f, Supplementary Information). The recovered energy can be used to power other electrical devices, such as lighting or heating/cooling systems. The polyviologen|Zn mesh and $WO_3 \cdot 2H_2O$ | Zn mesh circuits produce open-circuit voltages (OCV) of 1.23 V and 1.05 V, respectively. When two identical devices are connected in series, an OCV greater than 2 V can be achieved, sufficient to power an LED light (1.8 V, 2.2 W, Fig. 5c and S10, Supplementary Information).

Notably, both circuits are capable of self-coloration and self-bleaching. By directly connecting the Zn mesh anode to either the polyviologen cathode or the $WO_3 \cdot 2H_2O$ cathode, the internal potential difference drives spontaneous redox reactions, completing the coloration within 5 s (Fig. 5d). After disconnecting the electrodes, the

https://doi.org/10.1038/s41467-025-64962-2

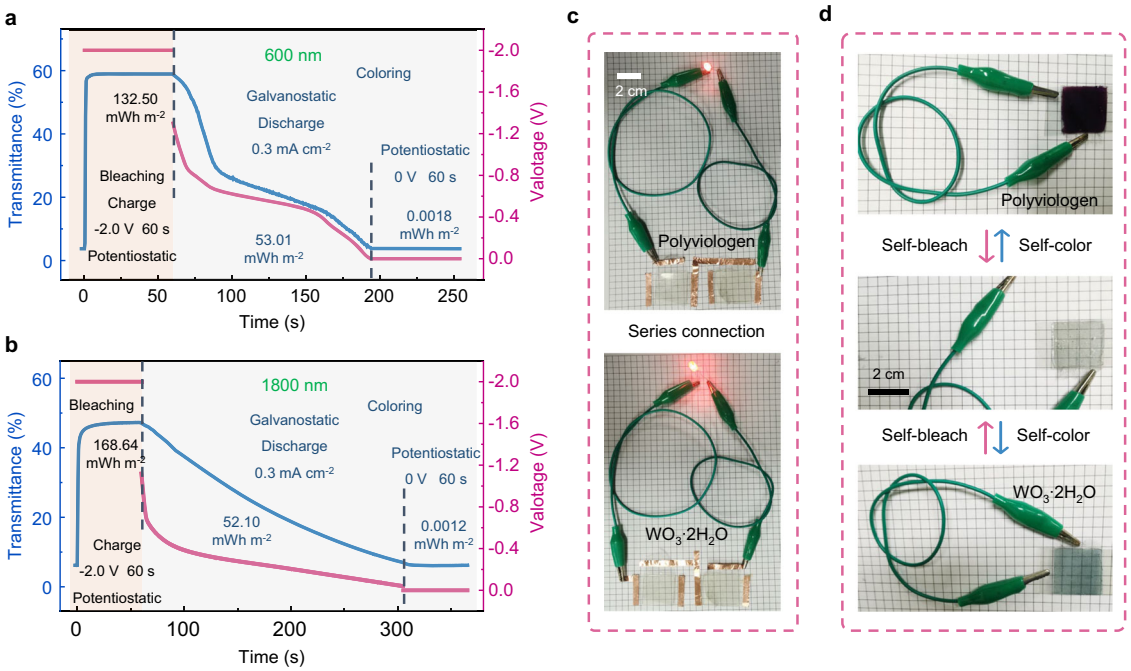

Fig. 5 | Energy consumption, energy recovery, and self-operating capability of the polyviologen|Zn mesh|$WO_3 \cdot 2H_2O$ EESDs. a Potentiostatic charge at −2.0 V for 60 s, galvanostatic discharge at 0.3 mA cm^{-2}, and potentiostatic charge at 0 V for 60 s between polyviologen and Zn mesh electrodes; and the corresponding changes of the transmittance at 600 nm. **b** Potentiostatic charge at −2.0 V for 60 s, galvanostatic discharge at 0.3 mA cm^{-2}, and potentiostatic charge at 0 V for 60 s between $WO_3 \cdot 2H_2O$ and Zn mesh electrodes; and the corresponding changes of the transmittance at 1800 nm. **c** Photographs of a red LED powered by two series-connected polyviologen|Zn mesh circuits (top) and two series-connected $WO_3 \cdot 2H_2O$ | Zn mesh circuits (bottom), respectively. **d** The photographs exhibiting the self-coloring and self-bleaching (middle) functions by connecting and disconnecting polyviologen|Zn mesh circuits (top) and $WO_3 \cdot 2H_2O$ | Zn mesh circuits (bottom), respectively.

device gradually undergoes complete self-bleaching within around 30 min. This cycle operates under zero energy consumption, further enhancing the device's energy-saving capability and contributing to the realization of net-zero energy buildings[52,53].

HVAC energy-saving capabilities as building smart windows

We analyzed the solar irradiance spectra of our device under different operating modes and calculated the corresponding Solar Heat Gain Coefficient (SHGC) values using Equations S1–S3 (Supplementary Information). The resulting SHGC values are as follows: fully transparent – 0.654, NIR colored – 0.564, visible colored – 0.348, and fully colored – 0.253. These findings highlight the device's strong ability to regulate solar radiation (Fig. 6a). Thanks to its dual-cathode configuration, the device supports bidirectional use based on weather demands (Fig. 6b). For example, under hot climates, the electrode with higher photothermal conversion efficiency can be oriented toward the exterior. The thermal conductivity of the surrounding materials significantly influences heat transfer, as indicated by Eqs. S4 and S5 in the Supplementary Information, which show that thinner layers facilitate faster thermal conduction. Accordingly, a 0.15 mm PET layer is placed on the exterior side to promote heat dissipation, while a thicker 0.6 mm PET layer is used on the interior side to minimize heat influx. Conversely, in cold climates, the device orientation can be reversed to enhance indoor heat retention. To quantify the photothermal conversion performance, we conducted laser-based photothermal measurements for both polyviologen and $WO_3 \cdot 2H_2O$ (Fig. 6c, d), yielding conversion efficiencies of 35.8% and 62.3%, respectively (Eqs. S6–S9, Tables S3 and S4). These distinct conversion efficiencies enable the device to perform optimally in diverse thermal environments, thereby broadening its usability across various climate zones.

To evaluate the potential of four-mode polyviologen|Zn mesh|$WO_3 \cdot 2H_2O$ EESDs as smart windows for buildings—capable of controlling dual-band light transmittance, regulating indoor temperature, and enhancing energy efficiency—we conducted a 24-hour outdoor real-world model test. As shown in Fig. 6e, we constructed a house model consisting of five identical rooms, each measuring 14 (L) × 14 (W) × 20 (H) cm^3. Each room had an identical upward-facing window equipped with a 10 × 10 cm^2 sized EESD in four different modes: transparent, visible colored, NIR colored, and fully colored, along with a PET film for comparison. The house model was positioned on the rooftop of an unobstructed building in Busan, South Korea, with the windows facing upward. A temperature logger was placed inside each room to record temperature data throughout the day on October 1, 2024 (sunny). The recorded minute-by-minute temperature variations in each room exhibited significant differences between 8:00 and 18:00 due to variations in solar radiation intensity and the window's ability to block radiation (Fig. 6f). At solar noon, around 12:34, the interior temperatures of the model rooms with PET film, transparent, visible colored, NIR colored, and fully colored modes as windows reached 71.3 °C, 70.0 °C, 53.7 °C, 66.4 °C, and 46.3 °C, respectively, while the outdoor ambient temperature (with walls fully shaded) was 37.9 °C. Figure 6g illustrates the temperature difference between the room and ambient temperatures using PET film and fully colored mode as the window at various local times. In the lower part of this figure, we also indicate the recommended usage times for the four modes. During midday, when solar radiation is intense, the fully colored mode helps lower the temperature and block the glaring sunlight. During dawn and dusk, the NIR-colored mode enhances brightness. At other times, the self-bleaching transparent mode can be activated to store energy efficiently. Additionally, visible light blocking can be applied at any time to ensure privacy as needed.

Along with the 24-hour outdoor real-world test, we also performed EnergyPlus building HVAC energy consumption simulations to assess the device's applicability for each month of the year, both in a

https://doi.org/10.1038/s41467-025-64962-2

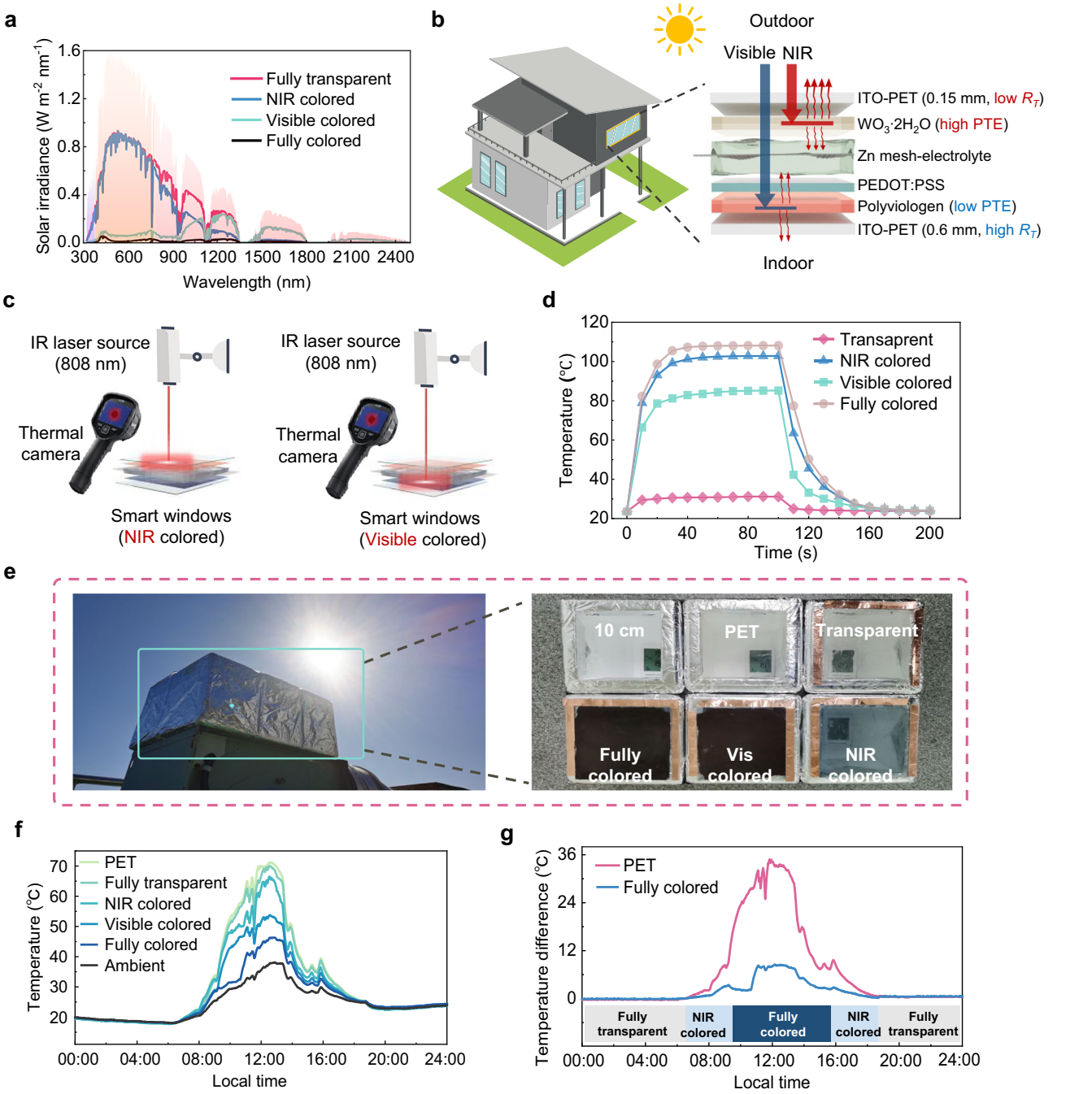

Fig. 6 | Photothermal control of the polyviologen|Zn mesh|$WO_3 \cdot 2H_2O$ EESD. **a** Solar irradiance spectra of the EESD at different states. **b** Schematic diagram of the light-heat conversion on the dual cathode as a smart window in operation. **c** Schematic illustration of testing the photothermal conversion efficiency (PTE) using the laser method (808 nm, 0.6 W), where the left is for the $WO_3 \cdot 2H_2O$ (NIR colored) layer and the right is for the polyviologen layer (visible colored) of the EESDs. **d** Laser method for testing the photothermal conversion efficiency (PTE) with heating up and cooling down curves. **e** Photographs of the thermal insulation test on October 1, 2024, in Busan, Korea, including the four states (self-colored) of the device and PET as the windows. **f** Ambient temperatures and corresponding real-time temperatures throughout the day in five room models. **g** Temperature differences between the different windows and the ambient surroundings.

specific city and across all U.S. states over the course of an entire year. We created a 40% window-to-wall ratio office model with typical office lighting, HVAC, and occupancy parameters (Table S5 and Fig. S9, Supplementary Information). The HVAC energy consumption for Phoenix, Arizona, was simulated monthly using climate data from the EnergyPlus website. Phoenix has distinct seasonal temperature variations, serving as a representative example to illustrate seasonal energy efficiency changes. The simulations compared commercial low-E glass (SunGuard® SNX 62/27 on Clear) and the polyviologen|Zn mesh|$WO_3 \cdot 2H_2O$ EESD as the sole variable window material, with the smart window set to operate in its most energy-efficient mode at various times and temperatures. The related data is presented in Fig. 7a and Table S6 (Supplementary Information). It was observed that the polyviologen|Zn mesh|$WO_3 \cdot 2H_2O$ EESD, in comparison to low-E glass, proved to be more energy-efficient throughout the year, achieving energy savings of 10%–15% during the winter months and saving 10–18 MJ m^{-2} during the summer months. Expanding the use of this smart window to other U.S. states, we simulated the annual building HVAC energy consumption in 16 cities representing typical climates across the country. The findings indicated comparable energy savings, with a

https://doi.org/10.1038/s41467-025-64962-2

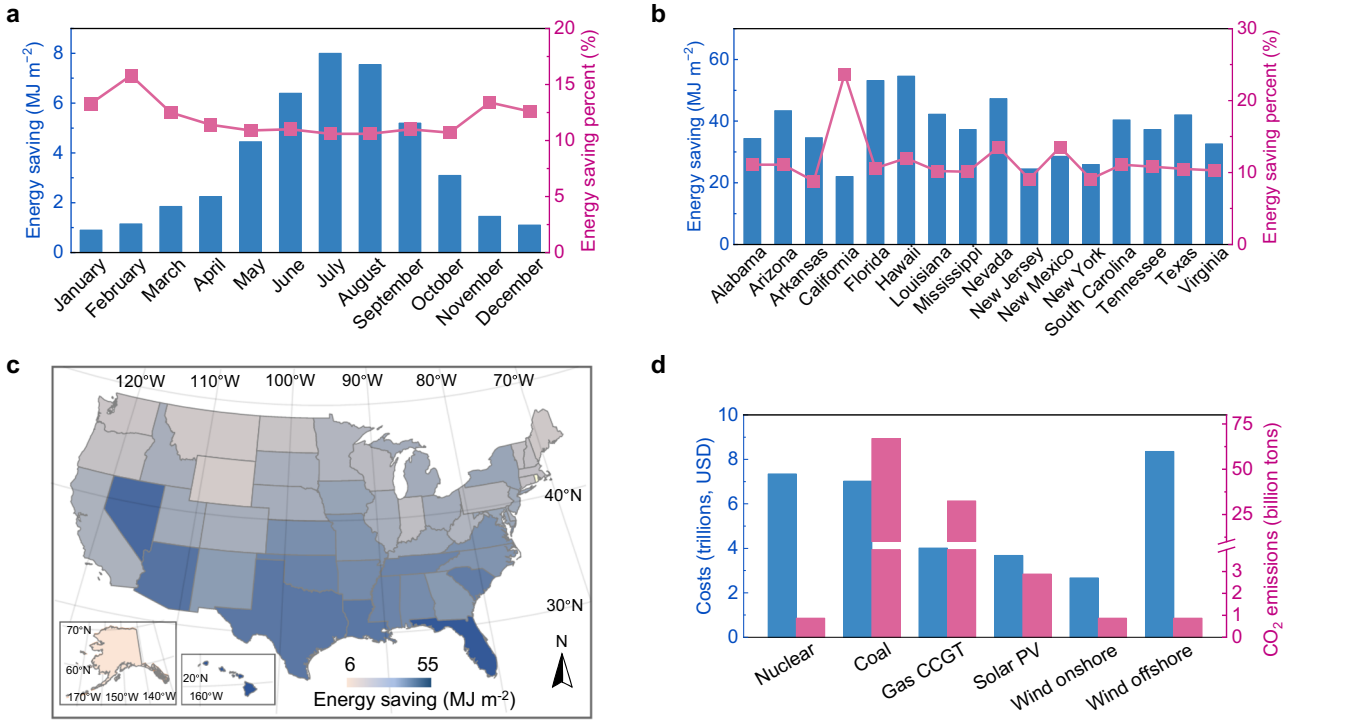

Fig. 7 | The all-time energy-saving capability of the polyviologen|Zn mesh|$WO_3 \cdot 2H_2O$ EESD. a Monthly operational HVAC energy saving and saving percent for buildings with this EESD compared to low-E glass in Phoenix, USA. **b** The annual HVAC energy savings and corresponding percentage of buildings using this EESD compared to low-E glass in 16 states of the United States. **c** Energy saving map of buildings using electrochromic devices compared to low-E glass across all 15 climate zones in the United States. **d** Energy savings in U.S. office buildings and their corresponding costs based on the levelized cost of electricity (LCOE) of various generation technologies, along with the associated CO_2 emissions from generating the corresponding amount of energy (CCGT: combined-cycle gas turbine, PV: photovoltaics).

40 MJ m^{-2} reduction accounting for more than 10% of the total annual HVAC energy consumption (Fig. 7b). Similar outcomes were obtained when implemented across the 50 U.S. states in 15 different climate zones, demonstrating the widespread feasibility of the smart window's energy-saving capabilities (Fig. 7c). The U.S. energy-saving map revealed a clear trend showing that the energy-saving effect is more significant in warmer regions at lower latitudes. This is attributed to the ability of the polyviologen|Zn mesh|$WO_3 \cdot 2H_2O$ EESD to block both light and thermal radiation.

Our smart windows provide substantial economic and environmental benefits, which can be clearly seen in the costs and carbon emissions related to the energy savings. As shown in Table S7 (Supplementary Information), the average energy savings across U.S. states is calculated to be 26.72 MJ m^{-2}. The U.S. Energy Information Administration (EIA) reported that the total commercial building area in the U.S. was about 97 billion square feet in 2018[54], allowing for a calculation of total energy savings across the country to be as high as 66.87 billion MWh. We have also obtained the levelized cost of electricity (LCOE) for different energy generation methods[55]. The economic costs of producing this large amount of electricity using nuclear, coal, gas, photovoltaic, onshore, and offshore wind power generation systems are estimated to range from $2.67 trillion to $7.35 trillion (Fig. 7d and Table S8, Eq. S10, Supplementary Information). By examining the carbon emissions per unit of electricity generated by various technologies[56], the carbon emissions associated with these energy savings can be calculated (Eq. S11, Supplementary Information). Even clean energy sources, like nuclear, photovoltaic, and wind, produce 0.87 billion tons of CO_2, while coal, a highly polluting energy source, has an astounding 66.94 billion tons of CO_2 emissions. These results, gathered from tests and simulations at various scales, demonstrate that this dual-electrode, four-mode smart window effectively reduces building HVAC energy consumption. It holds significant economic and environmental value, aiding in energy conservation, emission reduction, and achieving net-zero energy buildings globally.

Discussion

In this study, we fabricated polyviologen|zinc mesh|$WO_3 \cdot 2H_2O$ electrochromic energy storage device (EESD), containing the PEDOT:PSS layer, greatly enhancing the redox activity of the polyviologen film while improving its operational stability. By integrating the PEDOT:PSS layer into the polyviologen|Zn mesh structure, we achieved enhanced electrochromic (EC) and energy storage performances, including response times of 1.6 s for coloration and 0.8 s for bleaching, an optical difference of 64.23%, coloration efficiency of 389.44 C cm^{-2}, capacity of 141.9 mAh m^{-2} at 0.5 mA cm^{-2}, and long-term cycling stability. The dual-cathode, four-mode, dual-band tunable EESDs maintained EC performance while demonstrating remarkable energy recovery rates of 44.4% and 31.0% in polyviologen|Zn mesh and Zn mesh|$WO_3 \cdot 2H_2O$ circuits, respectively. The EESD supported fully power-free operation through self-coloration (5 s) and self-bleaching (30 min), making it a genuinely electricity-independent EC smart window. The four-mode smart window achieved a temperature reduction of up to 25 °C during outdoor testing. Compared to low-E glass, this EESD excelled in intelligent light and heat management, delivering energy-saving benefits year-round. The smart window consistently displayed higher energy efficiency across all states in the U.S., with an average value of 26.72 MJ m^{-2}. If implemented nationwide in office buildings, it is estimated to save 66.87 billion MWh of electricity. Depending on the power generation methods, the savings would translate into electricity costs ranging from $2.67 trillion to $7.35 trillion and a reduction in carbon emissions of between 0.87 billion and 66.94 billion tons. This work introduces an innovative, high-performance polyviologen EESD

architecture with broad potential applications and significant practical advantages for improving building energy efficiency.

Methods

Materials

The synthesis and characterization of polyviologen and precursor monomers are shown in Supplementary Information (Fig. S10–S12). $WO_3 \cdot 2H_2O$ was synthesized and characterized based on relevant reports[46] (details on page S17 and Fig. S13 of Supplementary Information). Stainless steel mesh (50 mesh, 0.0012″ wire diameter) was purchased from TWP Inc. Zinc mesh was fabricated according to previously reported methods, and detailed processes have been listed in pages S18-S19 of Supplementary Information (Fig. S14 and S15)[35].

Indium tin oxide coated polyethylene terephthalate (ITO-PET), with sheet resistances of 10, 30, and 50 Ω/□, was provided by Wooyang GMS (Korea). PEDOT:PSS (1.3 wt% dispersion in water, Clevios pH 1000) was purchased from Heraeus. 4,4′-Bipyridine (Sigma-Aldrich, >98.0%), 2-Bromoethylamine hydrobromide (TCI, >98.0%), Ammonium hexafluorophosphate (NH_4PF_6, TCI, >98.0%), hexamethylene diisocyanate (TCI, >98.0%), 2-acrylamido-2-methylpropanesulfonic acid (AMPS, TCI, >98.0%), acrylamide (Sigma-Aldrich, electrophoresis grade), zinc chloride ($ZnCl_2$, Sigma-Aldrich, ≥97%), N,N′-methylenebis(acrylamide) (MBAA, Sigma-Aldrich, 99%), 2-hydroxy-4′-(2-hydroxyethoxy)−2-methylpropiophenone (Irgacure 2959, Sigma-Aldrich, 98%), zinc sulfate heptahydrate (Sigma-Aldrich, ≥99.0%), sodium sulfate (Sigma-Aldrich, ≥99.0%), boric acid (Sigma-Aldrich, ≥99.5%), poly(ethyleneimine) solution (PEI, Sigma-Aldrich, analytical standard, 50% wt. in H_2O), Sodium tungstate dihydrate ($Na_2WO_4{\cdot}2H_2O$, Sigma-Aldrich, ≥99.0%), oxalic acid ($H_2C_2O_4$, TCI, >98.0%), dimethyl sulfoxide (DMSO, Sigma-Aldrich, ≥99.9%), glycerol (Sigma-Aldrich, ≥99.5%), ethylene glycol (Sigma-Aldrich, ≥99.8%), dodecylbenzenesulfonic acid (DBSA, TCI, >95.0%), and 1,4-butanediol divinyl ether (DVS, TCI, >98.0%) were used without further purification. The dialysis membrane (Molecular weight cut-off: 14,000) was obtained from Sigma-Aldrich (D9527), and anhydrous N,N-dimethylformamide (DMF, 99.8%) was used as the solvent for polymerization.

Fabrication of polyviologen, PEDOT:PSS, and $WO_3 \cdot 2H_2O$ films

ITO-PET was cleaned with deionized water, acetone, and isopropyl alcohol for 20 min under sonication and dried under a nitrogen purge. It was then irradiated with ultraviolet ozone (UVO) for 30 min to obtain a hydrophilic surface. ITO-PET/polyviologen: polyviologen was dissolved in acetone to prepare a solution with a concentration of 10 g L^{-1}. Using a spray gun, the solution was uniformly applied to ITO-PET on a heating plate at 80 °C. After further heating and drying for 30 minutes, a polyviologen film with a thickness of 3.9 μm was obtained on ITO-PET. ITO-PET/polyviologen/PEDOT:PSS: a PEDOT:PSS layer with a thickness of 80 nm was coated onto the ITO-PET/polyviologen via spray coating. To prepare PEDOT:PSS layer, 10 g of PEDOT:PSS, 2.5 g DMSO, 1 g glycerol, 0.5 mL ethylene glycol, 20 μL DVS, and 0.05 mL DBSA were mixed and stirred for 2 h at room temperature[57]. The solution is diluted 10 times and sprayed at 100 °C. ITO-PET/$WO_3 \cdot 2H_2O$: spin-coat a 10 g L^{-1} solution of the $WO_3 \cdot 2H_2O$ in ethyl alcohol onto the ITO glass five times, and then dry at 60 °C in air[46].

Preparation of electrolyte and electrolyte-coated zinc mesh

The UV-curable hydrogel electrolyte was prepared by dissolving 1 M AMPS as the negatively charged monomer, 1 M acrylamide as the neutral monomer, 2 M $ZnCl_2$ as the salt source, 0.05 mol% MBAA as the crosslinker, and 0.1 mol% Irgacure 2959 as the UV initiator in deionized water. The mixture was then stirred thoroughly until a clear solution was formed.

Electrolyte-coated zinc mesh: as shown in Fig. S16, the zinc mesh was initially fixed onto the glass using adhesive tape, with a 180 μm gap at both the top and bottom. Next, the prepared UV-curing electrolyte was applied, and the glass was covered to cure for 3 min. Finally, the glass and adhesive tape were removed to obtain a zinc mesh coated with the solid-state electrolyte. (Zinc mesh thickness: 36 μm, electrolyte thickness on both sides: 180 + 180 = 360 μm, total thickness: 396 μm.)

Electrochromic device fabrication

As illustrated in Fig. S17, the fabrication process for all three types of devices is the same and straightforward. Specifically, the prepared electrodes were directly applied to the top and bottom of the pre-coated zinc mesh with electrolyte. After gently pressing and securing the electrodes with glass, the device edges were sealed with AB epoxy resin. Due to its strong absorption in the NIR region, low-resistance ITO (10 Ω/□) has been limited to device applications for visible light modulation. In contrast, ITO-PET, with a sheet resistance of 50 Ω/□, was chosen for fabricating the dual-cathode, dual-band smart window, as it offers high transmittance across the entire spectral range (Fig. S18, Supplementary Information).

Photothermal experiments

An IR semiconductor laser (808 nm, 0.6 W) was employed to irradiate the devices under various conditions for 100 s. Temperature measurements were taken every 10 s using a high-resolution FLIR E-Series infrared camera. Following the irradiation period, the laser was turned off, and the devices were allowed to cool naturally at room temperature for another 100 s, with temperatures recorded at the same intervals. Photothermal conversion efficiency was calculated based on the recorded temperature profiles and related parameters, as detailed in the Supplementary Information (Pages S28–S30).

Property characterization

Nyquist impedance plots were obtained by plotting Re(Z)/ohm vs. Im(Z)/ohm, from which the ionic conductivity was calculated according to the Nyquist equation[58]. The polymer and zinc mesh morphologies were examined using a scanning electron microscope (SEM, Supra 40VP, Carl Zeiss). Electrochemical and spectroelectrochemical measurements were taken in a two-electrode system using an electrochemical workstation and a UV-3600 UV-Vis spectrophotometer (Shimadzu). The optical spectra of all devices and materials were measured with air as the reference background, except for several films where otherwise indicated. Essential parameters in evaluating the electrochromic performance, including the percent transmittance contrast (ΔT), the charge in optical density (ΔOD), and the coloration efficiency (CE), were calculated with the following formulas: $\Delta T = T_{max} - T_{min}$, $\Delta OD = \log \frac{T_{max}}{T_{min}}$, and $CE = \frac{\Delta OD}{Q_d}$, where T_{max} and T_{min} are the bleached and colored transmittance, respectively, and Q_d is the injected charge per unit area[59]. The switching time is defined as the time required to realize 95% of the transmittance difference at a given wavelength. Integrated optical transmittance (T) and integrated solar irradiance transmittance (T') of the polyviologen|Zn mesh|$WO_3 \cdot 2H_2O$ EESD at four states for visible (380–780 nm), NIR (780–2500 nm), and entire solar spectrum (380–2500 nm) are calculated based on the equation: $T = \frac{\int T(\lambda) d\lambda}{\int d\lambda}$, and $T' = \frac{\int T(\lambda)\psi(\lambda) d\lambda}{\int \psi(\lambda) d\lambda}$, where $T(\lambda)$ is the transmittance at wavelength λ, and $\psi(\lambda)$ is the solar irradiance at 1.5 air mass. The consumed and released energy (W) is calculated based on the equation: $W = \int U(t)I(t)dt$, where $U(t)$ is the voltage, $I(t)$ is the current, and t is time, respectively. Detailed calculations of the thermal conductivity and photothermal conversion efficiency (PTE) for the devices are provided in the Supplementary Information (Pages S27–S30).

The contribution of EESD windows to reducing HVAC energy consumption in buildings was determined through simulation using the EnergyPlus software. A building model of 20 m (L) × 10 m (W) × 3 m

(H) with twelve 3 m (W) × 2 m (H) glazed windows was adopted with a window-to-wall ratio of 40%. A year-long simulation of monthly building energy consumption was performed for Phoenix, Arizona, along with an annual analysis of building energy consumption across various climate zones in all 50 U.S. states to investigate regional impacts. The city's meteorological data were obtained from the EnergyPlus website. The fundamental parameters used in the simulation are listed in Table S5. The HVAC system was meticulously designed in the simulation, incorporating typical operation and occupancy schedules while accounting for all loads, including equipment, occupants, and lighting. The energy-saving performance of the building windows was determined by measuring the numerical differences between this EESD and commercial low-E glass. The spectral data for the respective window glazing materials are presented in Table S9 (Supplementary Information).

Data availability

All data supporting the results of this study are available in the paper and the Supplementary Information. Additional data related to this work are available from the corresponding authors upon request. Source data are provided as a Source Data file. Source data are provided with this paper.

References

1. Pérez-Lombard, L., Ortiz, J. & Pout, C. A review on buildings energy consumption information. *Energy Build.* **40**, 394–398 (2008).
2. Hee, W. J. et al. The role of window glazing on daylighting and energy saving in buildings. *Renew. Sustain. Energy Rev.* **42**, 323–343 (2015).
3. Ke, Y. et al. Smart windows: electro-, thermo-, mechano-, photochromics, and beyond. *Adv. Energy Mater.* **9**, 1902066 (2019).
4. Pugliese, M. et al. Visible light–near-infrared dual-band electrochromic device. ACS Sustain. *Chem. Eng.* **11**, 9601–9612 (2023).
5. Wang, Q. et al. Robust and stable dual-band electrochromic smart window with multicolor tunability. *Mater. Horiz.* **10**, 960–966 (2023).
6. Zhai, Y. et al. Recent advances on dual-band electrochromic materials and devices. *Adv. Funct. Mater.* **32**, 2109848 (2022).
7. Wang, J., Wang, Z., Zhang, M., Huo, X. & Guo, M. Toward next-generation smart windows: an in-depth analysis of dual-band electrochromic materials and devices. *Adv. Opt. Mater.* **12**, 2302344 (2024).
8. Zhuang, D. et al. Amorphous hydrated tungsten oxides with enhanced pseudocapacitive contribution for aqueous zinc-ion electrochromic energy storage. *Adv. Energy Mater.* **14**, 2402603 (2024).
9. Zhao, Q. et al. Electrochromic-induced rechargeable aqueous batteries: an integrated multifunctional system for cross-domain applications. *Nano-Micro Lett.* **15**, 87 (2023).
10. Pal, R. et al. Superior electrocatalytic responses of InGaZnO composite electrode for viologen-based electrochromic supercapacitors. *Compos. Part B-Eng.* **302**, 112557 (2025).
11. Chen, J. et al. The birth of zinc anode-based electrochromic devices. *Appl. Phys. Rev.* **11**, 011316 (2024).
12. Ma, D. et al. Quadruple control electrochromic devices utilizing Ce4W9O33 electrodes for visible and near-infrared transmission intelligent modulation. *Adv. Sci.* **11**, 2307223 (2024).
13. Chen, J. et al. A multi-color four-mode electrochromic window for all-season thermal regulation in buildings. *Adv. Energy Mater.* n/a, 2403414.
14. Zhang, W., Li, H., Yu, W. W. & Elezzabi, A. Y. Transparent inorganic multicolour displays enabled by zinc-based electrochromic devices. *Light Sci. Appl.* **9**, 121 (2020).
15. Li, H., Firby, C. J. & Elezzabi, A. Y. Rechargeable aqueous Hybrid Zn2 + /Al3+ electrochromic batteries. *Joule* **3**, 2268–2278 (2019).
16. Pal, R. et al. Photo-annealed electrospun TiO2 nanofibers as ion-storage layer for self-rechargeable Zn-based electrochromic energy storage device. *J. Power Sources* **621**, 235308 (2024).
17. Xie, Y. et al. Reusing the wasted energy of electrochromic smart window for near-zero energy building. *Adv. Sci.* **11**, 2406232 (2024).
18. Pande, G. K. et al. RGB-to-black multicolor electrochromic devices enabled with viologen functionalized polyhedral oligomeric silsesquioxanes. *Chem. Eng. J.* **420**, 130446 (2021).
19. Ambrose, B., Naresh, R., Deshmukh, S., Kathiresan, M. & Ragupathy, P. Exploring contemporary advancements and outlook in viologen-based aqueous organic redox flow batteries: a mini review. *Energy Fuels* **37**, 18226–18242 (2023).
20. Kathiresan, M. et al. Viologens: a versatile organic molecule for energy storage applications. *J. Mater. Chem. A* **9**, 27215–27233 (2021).
21. Madasamy, K., Velayutham, D., Suryanarayanan, V., Kathiresan, M. & Ho, K.-C. Viologen-based electrochromic materials and devices. *J. Mater. Chem. C.* **7**, 4622–4637 (2019).
22. Sun, F. et al. Large-area flexible electrochromic devices with high-performance and low-power consumption enabled by hydroxyhexyl viologen-substituted polyhedral Oligomeric Silsesquioxane. ACS Sustain. *Chem. Eng.* **11**, 5756–5763 (2023).
23. Gopal, B., Pal, R. & Park, J. S. Visible to near-infrared broadband electrochromic switching of π-extended viologen exhibiting highly efficient photothermal conversion. *Chem. Eng. J.* **408**, 148191 (2024).
24. Sun, F. et al. Stretchable interconnected modular electrochromic devices enabled by self-healing, self-adhesive, and ion-conducting polymer electrolyte. *Chem. Eng. J.* **494**, 153107 (2024).
25. Wu, W. et al. Viologen-based flexible electrochromic devices. *J. Energy Chem.* **93**, 453–470 (2024).
26. Pal, R., Sun, F., Yeon Kim, D. & Park, J. S. Dual-functional electrochromic supercapacitors with electrospun TiO2 ion storage layer. *J. Ind. Eng. Chem.* **132**, 270–278 (2024).
27. Kim, E. et al. Self-healing waterborne polyurethanes as a sustainable gel electrolyte for flexible electrochromic devices. *Adv. Eng. Mater.* **26**, 2400993 (2024).
28. Tajmoradi, Z., Roghani-Mamaqani, H., Asadpour-Zeynali, K. & Salami-Kalajahi, M. Electrochromic windows and flexible devices based on viologen-containing hydrogel electrolytes. *Microchem. J.* **207**, 111698 (2024).
29. Li, G. et al. Electrochromic Poly(chalcogenoviologen)s as Anode Materials for High-Performance Organic Radical Lithium-Ion Batteries. *Angew. Chem.* **131**, 8556–8561 (2019).
30. Ma, T., Liu, L., Wang, J., Lu, Y. & Chen, J. Charge storage mechanism and structural evolution of viologen crystals as the cathode of lithium batteries. *Angew. Chem. Int. Ed.* **59**, 11533–11539 (2020).
31. He, X., Chen, L. & Baumgartner, T. Modified Viologen- and Carbonylpyridinium-based electrodes for organic batteries. *ACS Appl. Mater. Interfaces* **16**, 48689–48705 (2024).
32. Liu, S.-M. et al. Influence of ferrocyanide on the long-term stability of poly(butyl viologen) thin film based electrochromic devices. *Sol. Energy Mater. Sol. Cells* **200**, 110012 (2019).
33. Wang, B., Tahara, H. & Sagara, T. Enhancement of deformation of redox-active hydrogel as an actuator by increasing pendant viologens and adding filler or counter-charged polymer. *Sens. Actuators B Chem.* **331**, 129359 (2021).
34. Shao, Z. et al. All-solid-state proton-based tandem structures for fast-switching electrochromic devices. *Nat. Electron.* **5**, 45–52 (2022).
35. Li, H., Zhang, W. & Elezzabi, A. Y. Transparent Zinc-mesh electrodes for solar-charging electrochromic windows. *Adv. Mater.* **32**, 2003574 (2020).

36. Wang, B. et al. An overview of recent progress in the development of flexible electrochromic devices. *Nano Mater. Sci.* **5**, 369–391 (2023).
37. Wu, W., Wang, M., Ma, J., Cao, Y. & Deng, Y. Electrochromic metal oxides: recent progress and prospect. *Adv. Electron. Mater.* **4**, 1800185 (2018).
38. Gu, S. et al. Effects of Ion Valence States and Radii on the Performance of Solid-State PEDOT:PSS Electrochromic Devices. *ACS Appl. Mater. Interfaces* **16**, 63978–63988 (2024).
39. Liu, Y. et al. Conjugated system of PEDOT:PSS-induced Self-Doped PANI for flexible zinc-ion batteries with enhanced capacity and cyclability. *ACS Appl. Mater. Interfaces* **11**, 30943–30952 (2019).
40. Wang, H., Zhao, Q., Li, W., Watanabe, S. & Wang, X. A dendrite-free Zn anode enabled by PEDOT:PSS/MoS2 electrokinetic channels for aqueous Zn-ion batteries. *Nanoscale* **16**, 7200–7210 (2024).
41. Gogotsi, Y. & Penner, R. M. Energy storage in nanomaterials – capacitive, pseudocapacitive, or battery-like?. *ACS Nano* **12**, 2081–2083 (2018).
42. Guo, J., Jia, H., Shao, Z., Jin, P. & Cao, X. Fast-switching WO3-based electrochromic devices: design, fabrication, and applications. *Acc. Mater. Res.* **4**, 438–447 (2023).
43. Yang, G. et al. Advances in nanomaterials for electrochromic devices. *Chem. Soc. Rev.* **49**, 8687–8720 (2020).
44. Kim, D. S. et al. A stretchable patch of multi-color electrochromic devices for driving integrated sensors and displaying bio-signals. *Nano Energy* **113**, 108607 (2023).
45. Chen, J., Eh, A. L.-S., Ciou, J.-H. & Lee, P. S. Pseudocapacitive and dual-functional electrochromic Zn batteries. Mater. *Today Energy* **27**, 101048 (2022).
46. Wang, Z. et al. Remarkable near-infrared electrochromism in tungsten oxide driven by interlayer water-induced battery-to-pseudocapacitor transition. *ACS Appl. Mater. Interfaces* **12**, 33917–33925 (2020).
47. Zhao, H. et al. Review on amorphous WO3 for electrochromic devices: Structure, optimization strategies and applications. *Mater. Today Chem.* **43**, 102513 (2025).
48. Zhou, Z., Chen, Z., Ma, D. & Wang, J. Porous WO3·2H_2O film with large optical modulation and high coloration efficiency for electrochromic smart window. *Sol. Energy Mater. Sol. Cells* **253**, 112226 (2023).
49. Huang, Y. et al. Electrochromic materials based on ions insertion and extraction. *Adv. Opt. Mater.* **10**, 2101783 (2022).
50. Bui, D.-K., Nguyen, T. N., Ghazlan, A. & Ngo, T. D. Biomimetic adaptive electrochromic windows for enhancing building energy efficiency. *Appl. Energy* **300**, 117341 (2021).
51. Xie, Y., Li, M., Huang, R., Cao, N. & Chao, D. How much of the energy in the electrochromic energy storage window can be reused?. *Energy Storage Mater.* **67**, 103321 (2024).
52. Wu, W. & Skye, H. M. Residential net-zero energy buildings: Review and perspective. *Renew. Sustain. Energy Rev.* **142**, 110859 (2021).
53. Mustafa, M. N. et al. Smart window technology and its potential for net-zero buildings: A review. *Renew. Sustain. Energy Rev.* **181**, 113355 (2023).
54. Energy Information Administration (EIA)- Commercial Buildings Energy Consumption Survey (CBECS). https://www.eia.gov/consumption/commercial/.
55. World Energy Outlook 2024 – Analysis. IEA https://www.iea.org/reports/world-energy-outlook-2024 (2024).
56. Life Cycle Greenhouse Gas Emissions from Electricity Generation: Update. https://www.osti.gov/biblio/1820320 (2021).
57. Eom, Y. S., Pal, R., Pande, G. K. & Park, J. S. Freely deformable electrochromic fabric devices exhibiting durable chromatic switching and all-around stability. *J. Electrochem. Soc.* **169**, 023509 (2022).
58. Ramanavicius, A., Finkelsteinas, A., Cesiulis, H. & Ramanaviciene, A. Electrochemical impedance spectroscopy of polypyrrole based electrochemical immunosensor. *Bioelectrochemistry* **79**, 11–16 (2010).
59. Pande, G. K., Sun, F., Kim, D. Y., Eom, J. H. & Park, J. S. Influence of ITO electrode on the electrochromic performance outcomes of viologen-functionalized polyhedral oligomeric silsesquioxanes. *RSC Adv.* **12**, 12746–12752 (2022).

Acknowledgements

This work was supported by the National Research Foundation of Korea (NRF) grant funded by the Korean government (MEST) (RS-2023-00208341 and RS-2023-00221396).

Author contributions

F.S. and J.S.P. conceived the idea. F.S. performed all the experiments and wrote the original manuscript. J.S.P. instructed and supervised the experiments and reviewed and edited the manuscript. R.P. participated in some of the electrochemical tests and revisions. S.Y.E. and W.Z. helped with the sample characterization tests. J.W.C. helped with the synthesis of the viologen monomers. B.J. participated in the analysis and discussion of the results. All authors have approved the final version of the paper.

Competing interests

The authors declare no competing interests.

Additional information

Supplementary information The online version contains supplementary material available at https://doi.org/10.1038/s41467-025-64962-2.

Correspondence and requests for materials should be addressed to Jong S. Park.

Peer review information *Nature Communications* thanks Marco Pugliese and the other, anonymous, reviewer(s) for their contribution to the peer review of this work. A peer review file is available.